



Cite this article: Wu-Zhang B, Zhang P, Baillou R, Lindner A, Clement E, Gompper G, Fedosov DA. 2025 Run-and-tumble dynamics of *Escherichia coli* is governed by its mechanical properties. *J. R. Soc. Interface* **22**: 20250035.
<https://doi.org/10.1098/rsif.2025.0035>

Received: 10 January 2025

Accepted: 24 March 2025

Subject Category:

Life Sciences—Physics interface

Subject Areas:

biophysics

Keywords:

bacterium model, hydrodynamic simulation, motility, navigation, propulsion

Author for correspondence:

Dmitry A. Fedosov

e-mail: d.fedosov@fz-juelich.de

Electronic supplementary material is available online at <https://doi.org/10.6084/m9.figshare.c.7742054>.

Run-and-tumble dynamics of *Escherichia coli* is governed by its mechanical properties

Bohan Wu-Zhang¹, Peixin Zhang², Renaud Baillou², Anke Lindner^{2,3}, Eric Clement^{2,3}, Gerhard Gompper¹ and Dmitry A. Fedosov¹

¹Theoretical Physics of Living Matter, Institute for Advanced Simulation, Forschungszentrum Jülich, Jülich 52425, Germany

²Laboratoire PMMH-ESPCI, UMR 7636 CNRS-PSL-Research University, Sorbonne Université, Université Paris Cité, Paris 75005, France

³Institut Universitaire de France, Paris, France

AL, 0000-0002-5007-9568; EC, 0000-0002-2068-9699; GG, 0000-0002-8904-0986; DAF, 0000-0001-7469-9844

The huge variety of microorganisms motivates fundamental studies of their behaviour with the possibility to construct artificial mimics. A prominent example is the *Escherichia coli* bacterium, which employs several helical flagella to exhibit a motility pattern that alternates between run (directional swimming) and tumble (change in swimming direction) phases. We establish a detailed *E. coli* model, coupled to fluid flow described by the dissipative particle dynamics method, and investigate its run-and-tumble behaviour. Different *E. coli* characteristics, including body geometry, flagella bending rigidity, the number of flagella and their arrangement at the body, are considered. Experiments are also performed to directly compare with the model. Interestingly, in both simulations and experiments, the swimming velocity is nearly independent of the number of flagella. The rigidity of a hook (the short part of a flagellum that connects it directly to the motor), polymorphic transformation (spontaneous change in flagella helicity) of flagella and their arrangement at the body surface strongly influence the run-and-tumble behaviour. Mesoscale hydrodynamics simulations with the developed model help us better understand physical mechanisms that govern *E. coli* dynamics, yielding the run-and-tumble behaviour that compares well with experimental observations. This model can further be used to explore the behaviour of *E. coli* and other peritrichous bacteria in more complex realistic environments.

1. Introduction

There exists a huge variety of microorganisms, which are part of nearly any environment, including air, water, soil and biological organisms. Microorganisms generally have micrometre dimensions, and many of them possess some type of motility. Motile microorganisms are often referred to as microswimmers, which propel themselves to explore the environment and search for nutrition. In a fluid environment, propulsion of biological microswimmers is often facilitated by external appendages attached to the body such as flagella and cilia [1–4]. Common examples are sperm cells with a beating flagellum [5], *Escherichia coli* bacteria propelled by several rotating flagella [6,7] and paramecia whose body is covered by a large number of hair-like active cilia [8]. The scientific interest in understanding the motile behaviour of microswimmers ranges from fundamental characterization of physical mechanisms of propulsion [1–3] to the construction of microrobotic systems mimicking various aspects of biological microswimmers [9,10].

An interesting biological microswimmer is the bacterium *E. coli*, which employs multiple helical flagella for propulsion [6]. A typical *E. coli* has a

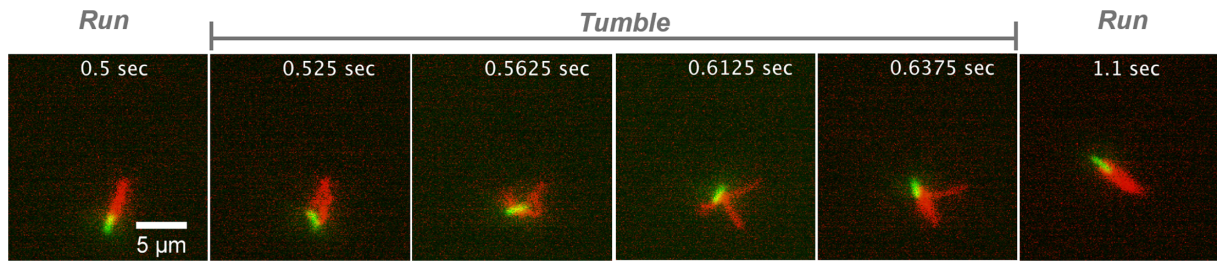


Figure 1. Experimental observation of typical run-and-tumble dynamics of *E. coli*. Bacterium body is fluorescently labelled in green, while flagella are labelled in red. The run phase is shown in the first and last panels, where all flagella are in a single tight bundle. The tumble phase is illustrated in the remaining panels, where one or several flagella leave the bundle. The scale is the same in all panels and is indicated by the scale bar of 5 μm . See also electronic supplementary material, video S1.

sphero-cylinder-like body with a length of $2.5 \pm 0.6 \mu\text{m}$ and a diameter of $0.88 \pm 0.09 \mu\text{m}$ [11], and typically between 2 and 7 helical flagella with a length of $8.3 \pm 2.0 \mu\text{m}$ [12] attached to the body. Each flagellum is driven by a reversible rotary motor placed within the base membrane [6,7]. When all flagella rotate in the same direction, they form a single bundle, which facilitates efficient forward propulsion. A wild-type *E. coli* bacterium has a swimming speed of $29 \pm 6 \mu\text{m s}^{-1}$ in an aqueous environment [11]. The synchronization between flagella and the formation of a tight bundle is facilitated by hydrodynamic interactions between flagella, as shown in several theoretical studies [13–16] and experiments [17,18]. Flagellar elasticity is also important for bundle formation, since it does not occur for rigid helices [15,16,19–23].

To explore the environment and change the swimming direction, *E. coli* bacteria employ a so-called ‘run-and-tumble’ motion (figure 1), which resembles a random walk [6,24]. During a run phase, all left-handed flagella rotate in the anti-clockwise direction and form a tight bundle that serves as a single helical propeller. Therefore, the run phase leads to a directed motion. In order to turn, *E. coli* bacteria ‘tumble’, where one or more flagella switch the rotation direction to clockwise and leave the bundle, facilitating a change in the swimming direction [25,26]. As a result, *E. coli* can navigate through the environment using an interchangeable sequence of longer directional runs and shorter tumble phases [25,27]. Note that in the presence of chemical gradients, the seemingly random run-and-tumble behaviour of *E. coli* may change with a substantial reduction in the tumbling frequency [28,29].

Even though the qualitative description of *E. coli* tumbling is fairly simple, its physical realization is more complex. Experimental observations show that the flagella of *E. coli* can have several different polymorphic forms, depending on their state during the run-and-tumble phases [11,25,26]. During the run phase, all flagella have a shape referred to as a ‘normal state’, which is a left-handed helix with a pitch of approximately $2.5 \mu\text{m}$ and a diameter of approximately $0.5 \mu\text{m}$. However, upon the start of the tumble phase, one or two of the flagella change their helicity from left-handed to right-handed with different helical properties (e.g. pitch and diameter), in addition to the alteration of rotation in the clockwise direction [25,26]; this is called a polymorphic transformation. At the end of the tumble phase, these reverted flagella change their rotation again from clockwise to anti-clockwise, thereby restoring the original state.

Another interesting aspect is the flexural rigidity of the flagellar hook, the short part of a flagellum that connects it directly to the motor. The hook plays an important role in flagella bundling and unbundling and thus contributes to the control of the swimming behaviour [30–32]. On the one hand, both theoretical and experimental studies [12,33,34] show that the hook must be sufficiently flexible to allow multi-flagellated bacteria to form a flagellar bundle. On the other hand, the hook must also be stiff enough to withstand forces exerted by the motor and aid clockwise-rotating flagella in their separation from the bundle during tumble events. Mechanical properties of the hook have been measured, yielding a torsional rigidity of approximately 10^7 Nm^{-2} and a bending rigidity of approximately 10^{-29} Nm^2 [35]. Other investigations [31,36,37] report changes in the bending rigidity of the hook, depending on the load applied by the motor. For a steady-swimming *E. coli*, a bending rigidity of $2.2 \times 10^{-25} \text{ Nm}^2$ was measured for the hook, while for a resting bacterium, the value of $3.6 \times 10^{-26} \text{ Nm}^2$ was reported [31]. Also, an increase in the hook bending rigidity from $5 \times 10^{-26} \text{ Nm}^2$ to $3 \times 10^{-24} \text{ Nm}^2$ was suggested with an increase in the motor torque [36]. A further study reports the hook to be stiffer when the motor rotates clockwise in comparison to the anti-clockwise rotation under similar motor torques [37].

Since the first observations of the run-and-tumble behaviour of wild-type *E. coli* [6], a number of experiments have been performed to quantify bacterial motion. The tumble angle, defined as a change in the swimming direction before and after a tumble event, was estimated to be in the range 62° – 68° for a tumble time of 0.2 s [6], while tumble angles of $57^\circ \pm 37^\circ$ for a tumble time of 0.19 s have been reported [38]. Furthermore, measurements of anti-clockwise/clockwise time series of a motor for wild-type *E. coli* estimate the time of clockwise rotation to be approximately 0.38 s [39]. Note that all these measurements may not have consistent definitions for the tumble angles and times.

To better understand experimental observations and the underlying mechanism, several simulation studies with detailed *E. coli* models have recently been performed [19,40–42]. In [40,41], only run dynamics of *E. coli* for different bacterium properties and near surfaces was investigated. The run-and-tumble behaviour was studied in [19,42], and an increasing tumble angle from 10° to 80° was observed for an increasing tumble time. However, numerical discretization of *E. coli* body and flagella was quite coarse. Furthermore, the question of how different bacterial characteristics, such as body geometry, flagella and hook bending rigidity and the polymorphic transformation, determine the run-and-tumble behaviour has not been directly considered.

In our work, we establish a detailed model of *E. coli* and investigate its run-and-tumble behaviour in comparison to experimental observations. We show that the body geometry (sphero-cylinder-like or spheroidal) strongly affects the balance between

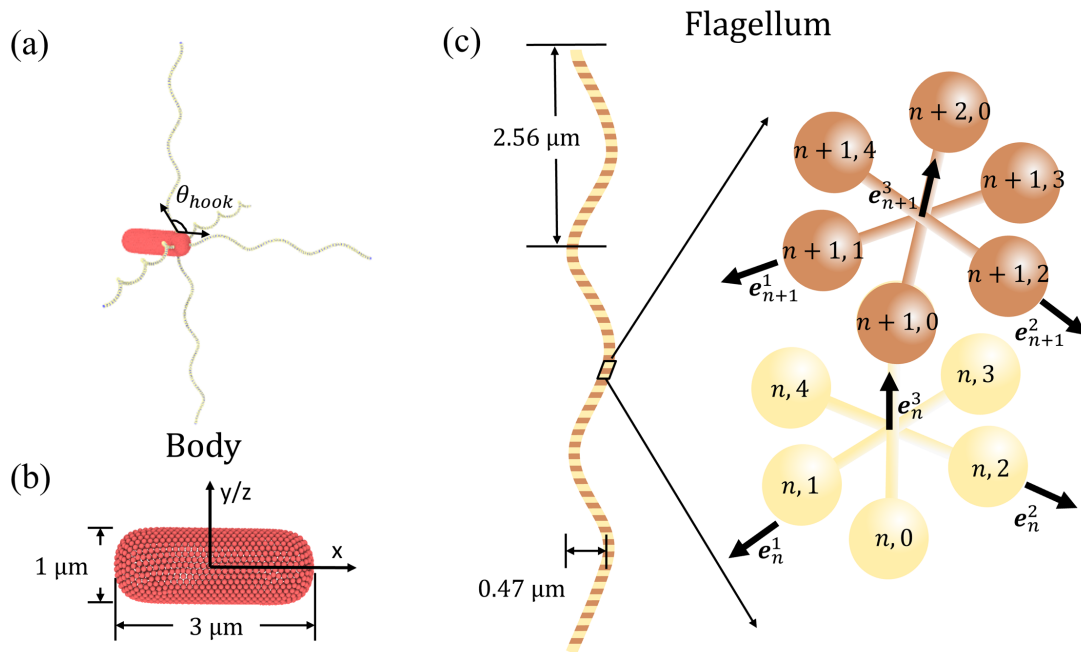


Figure 2. (a) *Escherichia coli* model that consists of a sphero-cylinder-like cell body and $N_{\text{flag}} = 5$ left-handed helical flagella. The hook angle θ_{hook} is illustrated and defined as the angle between the first section of a flagellum and the body surface. (b) Sphero-cylinder-like cell body described by equation (2.1) has a length of 3 μm and a diameter of 1 μm . It is represented by a collection of 1278 particles, forming a triangulated spring network on its surface. (c) Model of a left-handed flagellum with three helical turns made of $N_s = 76$ segments. It has a diameter of 0.47 μm and a pitch length of 2.56 μm . The flagellum model is adopted from [40].

rotational frequencies of the body and flagellar bundle, which may significantly limit successful tumbling of *E. coli*. Furthermore, both the polymorphic transformation and the stiffening of the hook of clockwise-rotating flagella are found to play important roles in an efficient change of the swimming direction. In particular, they govern the efficient separation of clockwise-rotating flagella from the bundle. Our model helps to better understand the importance of different *E. coli* characteristics for the run-and-tumble behaviour, which is qualitatively consistent with the corresponding experimental observations. In the experiments, a novel two-colour three-dimensional (3D) Lagrangian tracking method [43] is employed for the observation of flagella configurations and dynamics of *E. coli* bacteria under free-swimming conditions in the bulk. Our computational model can further be used to investigate the behaviour of *E. coli* and other peritrichous bacteria in complex environments, such as near surfaces and in complex geometries.

2. Methods and models

2.1. *Escherichia coli* model

Our *E. coli* model is composed of the following two parts: (i) a rounded sphero-cylinder-like cell body and (ii) N_{flag} left-handed helical flagella (figure 2). The surface of the cell body, aligned with the x axis, is described by

$$\left(\frac{|x|}{b_x}\right)^\nu + \left(\frac{y}{b_y}\right)^2 + \left(\frac{z}{b_z}\right)^2 = 1, \quad (2.1)$$

where $\nu = 8.5$ for a sphero-cylinder-like shape, $b_x = 1.5 \mu\text{m}$ is the major half-axis and $b_y = b_z = 0.5 \mu\text{m}$ is the minor half-axis, following the aspect ratio of $b_x/b_y \approx 2-3$ for wild *E. coli* [11]. The body surface is represented by $N_v = 1278$ point particles that form an elastic triangulated network through bonds with a non-linear potential [44,45]

$$U_{\text{bond}} = \sum_i \frac{k_B T l_i^{\text{max}}}{4p} \frac{3x_i^2 - 2x_i^3}{1 - x_i} + \frac{k_p}{l_i}, \quad (2.2)$$

where $x_i = l_i/l_i^{\text{max}} \in (0, 1)$, l_i is the length of bond i , $l_i^{\text{max}} = l_i^0/x_0$ is the maximum extension of spring i , l_i^0 is the spring length from an initial triangulation of the body and $x_0 = 0.45$ is a constant for all springs. Furthermore, p is the persistence length, k_p is the repulsive force coefficient and $k_B T$ is the thermal energy unit defined by the temperature T of the simulated system.

In addition to the shear elasticity imposed by U_{bond} , the body shape is further stabilized by a curvature elasticity implemented through the Helfrich bending energy [46] discretized as [47,48]

$$U_{\text{bend}} = \frac{\kappa}{2} \sum_i \sigma_i (H_i - H_i^0)^2 = \frac{\kappa}{2} \sum_i \sigma_i \left(\mathbf{n}_i \cdot \sum_{j(i)} \frac{\sigma_{ij} \mathbf{r}_{ij}}{\sigma_i r_{ij}} - H_i^0 \right)^2, \quad (2.3)$$

where κ is the membrane bending rigidity, σ_i is the area of particle i in a dual lattice, H_i is the mean curvature at vertex i and H_i^0 is the local spontaneous curvature. $\sigma_i = \sum_{j(i)} \sigma_{ij} r_{ij}/4$, where $j(i)$ spans all vertices linked to vertex i , $\sigma_{ij} = r_{ij}(\cot \theta_1 + \cot \theta_2)/2$ is the length of the bond in the dual lattice with θ_1 and θ_2 being the angles at the two vertices opposite to the edge ij in the dihedral. Furthermore, $\mathbf{r}_{ij} = \mathbf{r}_i - \mathbf{r}_j$, $r_{ij} = |\mathbf{r}_{ij}|$, and \mathbf{n}_i is the unit normal at the vertex i . Note that the spontaneous curvature H_i^0 is prescribed locally after the triangulation of the body surface.

Conservation of the area and volume of the body is controlled by the potential [44,45]

$$U_{a+v} = \frac{k_a(A - A_0^{\text{tot}})^2}{2A_0^{\text{tot}}} + \sum_{m \in 1 \dots N_t} \frac{k_d(A_m - A_m^0)^2}{2A_m^0} + \frac{k_v(V - V_0^{\text{tot}})^2}{2V_0^{\text{tot}}}, \quad (2.4)$$

where k_a , k_d and k_v are the coefficients of global area, local area and volume conservation constraints. A and V are the instantaneous area and volume of the body surface, A_0^{tot} and V_0^{tot} are the targeted global area and global volume which are set to those of the selected spherocylinder-like shape. A_m is the area of the m th triangle (or face), while A_m^0 is its targeted value. N_t is the number of triangles within the triangulated surface. Note that the model described by the potentials above has been used to represent deformable and nearly rigid particles of various shapes [44,49,50].

The flagellum model is borrowed from [40]. Figure 2c illustrates a left-handed helical flagellum comprised of $N_s = 76$ segments with 381 particles in total. Each segment consists of six particles arranged in a regular octahedral structure, stabilized by 12 springs with an equilibrium length of $r_e = 0.06b_x/\sqrt{2}$. Opposite particles within the octahedral arrangement are connected by three diagonal springs with a preferred bond length of $r_d = 0.06b_x$. The octahedral construction of a flagellum allows a straightforward imposition of the inherent helical twist and facilitates a better coupling of the flagellum to the particle-based fluid.

The flagellar backbone is determined by the bonds $\mathbf{b}_n^3 = \mathbf{r}_{n+1,0} - \mathbf{r}_{n,0}$, where $n = 1 \dots N$. The backbone bonds, along with $\mathbf{b}_n^1 = \mathbf{r}_{n,1} - \mathbf{r}_{n,3}$ and $\mathbf{b}_n^2 = \mathbf{r}_{n,2} - \mathbf{r}_{n,4}$, establish the corresponding orthonormal triads $\{\mathbf{e}_n^1, \mathbf{e}_n^2, \mathbf{e}_n^3\}$, where $\mathbf{e}_n^\alpha = \mathbf{b}_n^\alpha / |\mathbf{b}_n^\alpha|$ with $\alpha \in \{1, 2, 3\}$. Here, $\mathbf{r}_{n,0}$ represents the positions of the backbone particles, while $\mathbf{r}_{n,k}$ with $k \in \{1, 2, 3, 4\}$ corresponds to the positions of the auxiliary particles lying in the plane perpendicular to the backbone vector \mathbf{b}_n^3 .

To capture the local twist and bending of the flagellum, transformation of one triad $\{\mathbf{e}_n^1, \mathbf{e}_n^2, \mathbf{e}_n^3\}$ to the next $\{\mathbf{e}_{n+1}^1, \mathbf{e}_{n+1}^2, \mathbf{e}_{n+1}^3\}$ along the backbone is performed in the following two steps: (i) first, $\{\mathbf{e}_n^1, \mathbf{e}_n^2, \mathbf{e}_n^3\}$ is rotated around \mathbf{e}_n^3 by a twist angle ϕ_n , and (ii) second, the twisted triad is rotated by a bending angle θ_n around the normal $\mathbf{n}_n = (\mathbf{e}_n^3 \times \mathbf{e}_{n+1}^3) / |\mathbf{e}_n^3 \times \mathbf{e}_{n+1}^3|$ to the plane defined by the backbone bonds \mathbf{b}_n^3 and \mathbf{b}_{n+1}^3 . Following these transformations, an elastic deformation energy of the helical flagellum is defined as

$$U_{el} = \frac{1}{2} \sum_{\alpha=1}^3 K_{el}^\alpha \sum_{n=1}^{N-1} (\Omega_n^\alpha - \Omega_e^\alpha)^2, \quad (2.5)$$

where $K_{el}^1 = K_{el}^2$ determine the bending rigidity and K_{el}^3 the twisting rigidity. $\Omega_n = \Omega_n^1 \mathbf{e}_n^1 + \Omega_n^2 \mathbf{e}_n^2 + \Omega_n^3 \mathbf{e}_n^3 = \theta_n \mathbf{n}_n + \phi_n \mathbf{e}_n^3$ is the strain vector. The equilibrium structure of the flagellum is defined by the Ω_e^α parameters in equation (2.5), which determine the helix radius and pitch length. Note that the handedness of the flagellum can simply be changed by altering the sign of Ω_e^1 and Ω_e^2 .

Each flagellum is attached to the body by making the first particle $\mathbf{r}_{1,0}$ of the flagellum backbone to be part of the body discretization. To impose anchoring orientation of the flagellum with respect to the body, an angle potential

$$U_{\text{hook}} = K_{\text{hook}} \sum_{j(i)} (\theta_j^{\text{hook}} - \pi/2)^2 \quad (2.6)$$

is employed, where K_{hook} is the potential strength, i is the anchoring particle at the body such that $\mathbf{r}_i = \mathbf{r}_{1,0}$, $j(i)$ spans all body vertices linked to vertex i and θ_j^{hook} is the angle between vectors $\mathbf{r}_j - \mathbf{r}_i$ and $\mathbf{r}_{2,0} - \mathbf{r}_i$. The preferred angle of anchoring orientation is chosen to be $\pi/2$, imposing a perpendicular orientation of the flagellum to the body. The potential U_{hook} mimics the rigidity of a flagellum hook, which is an initial short part (50–60 nm in length) of the flagellum that is generally softer than the rest of the flagellum [31,51]. Thus, K_{hook} represents the bending rigidity of the physical hook and will be referred to as hook rigidity below.

The action of a motor imposing flagellum rotation is implemented by a torque \mathbf{T}_m , which is aligned with \mathbf{b}_1^3 , and exerted onto the particles $1, k$ ($k \in \{1, 2, 3, 4\}$) of the first segment of the flagellum. To satisfy torque-free and force-free conditions for the swimmers, a counter torque $-\mathbf{T}_m$ is imposed onto the body particles $j(i)$. Finally, excluded-volume interactions between different flagella and between flagella and the body surface are implemented using the repulsive part of the Lennard-Jones (LJ) potential as

$$U_{\text{LJ}}(r) = 4\epsilon_{\text{LJ}} \left[\left(\frac{\sigma_{\text{LJ}}}{r} \right)^{12} - \left(\frac{\sigma_{\text{LJ}}}{r} \right)^6 + \frac{1}{4} \right], \quad r \leq 2^{1/6} \sigma_{\text{LJ}}, \quad (2.7)$$

where ϵ_{LJ} sets the strength of the potential, σ_{LJ} is the characteristic repulsion length and r is the distance between two interacting particles.

2.2. Modelling fluid flow

Fluid flow is modelled by the dissipative particle dynamics (DPD) method, a mesoscopic hydrodynamics simulation technique [52,53]. The DPD fluid consists of a collection of particles, each representing a small fluid volume. DPD particles i and j interact

through three pair-wise forces (conservative, dissipative and random)

$$\mathbf{F}^C(r_{ij}) = a_{ij}(1 - r_{ij}/r_c)\hat{\mathbf{r}}_{ij}, \quad (2.8)$$

$$\mathbf{F}^D(r_{ij}) = -\gamma w^D(r_{ij})(\hat{\mathbf{r}}_{ij} \cdot \mathbf{v}_{ij})\hat{\mathbf{r}}_{ij}, \quad (2.9)$$

$$\mathbf{F}^R(r_{ij}) = \sigma w^R(r_{ij})\xi_{ij}\hat{\mathbf{r}}_{ij}/\sqrt{\Delta t}, \quad (2.10)$$

where a , γ and σ determine the force strengths, $\mathbf{r}_{ij} = \mathbf{r}_i - \mathbf{r}_j$ is the distance vector, $r_{ij} = |\mathbf{r}_{ij}|$, $\hat{\mathbf{r}}_{ij} = \mathbf{r}_{ij}/r_{ij}$ and $\mathbf{v}_{ij} = \mathbf{v}_i - \mathbf{v}_j$ is the velocity difference. Δt is the time step, and $\xi_{ij} = \xi_{ji}$ is the symmetric Gaussian random variable with zero mean and unit variance. The dissipative \mathbf{F}^D and random \mathbf{F}^R forces define a thermostat and are related to each other through the fluctuation-dissipation theorem [53] as

$$\sigma^2 = 2\gamma k_B T, \quad w^D(r_{ij}) = [w^R(r_{ij})]^2, \quad (2.11)$$

with the weight function $w^R(r_{ij})$:

$$w^R(r_{ij}) = \begin{cases} (1 - r_{ij}/r_c)^s, & r_{ij} < r_c, \\ 0, & r_{ij} \geq r_c, \end{cases} \quad (2.12)$$

where the exponent s controls the decay of $w^R(r_{ij})$ as a function of inter-particle distance. All forces vanish beyond the cutoff radius r_c .

The repulsive force \mathbf{F}^C controls fluid compressibility, while the dissipative force \mathbf{F}^D reduces the velocity difference between two neighbouring particles, controlling fluid viscosity. The positions and velocities of DPD particles are updated using Newton's second law:

$$\frac{d\mathbf{r}_i}{dt} = \mathbf{v}_i, \quad m_i \frac{d\mathbf{v}_i}{dt} = \sum_{j \neq i} (\mathbf{F}^C(r_{ij}) + \mathbf{F}^D(r_{ij}) + \mathbf{F}^R(r_{ij})), \quad (2.13)$$

where m_i is the mass of particle i . The time integration in our simulations is performed using the velocity-Verlet algorithm [54].

2.3. Simulation set-up and parameters

We define a length scale as the length of the major half-axis b_x ($b_x = 9$ in simulation units), a time scale τ ($\tau = 132$ in simulation units) as the period of bundle rotation and an energy scale as $k_B T$ ($k_B T = 1$ in all simulations). Simulations are performed in a domain with dimensions $8.33b_x \times 11.56b_x \times 11.56b_x$, where periodic boundary conditions are imposed in all three directions. Each simulation contains a single bacterium and 2.4×10^6 fluid particles with a number density of $n_d = 2.16 \times 10^3 b_x^{-3}$. Particle number density defines how fine the fluid is discretized, with a characteristic discretization length $\approx (1/n_d)^{1/3}$, which is close to the discretization length l^0 of the *E. coli* body and flagella. DPD parameters for interactions between fluid particles are $a = 540k_B T/b_x$, $\gamma = 225\sqrt{mk_B T}/b_x$, $s = 0.15$ and $r_c = 0.11b_x$ ($m = 1$ in all simulations). These parameters result in a dynamic viscosity of $\eta = 1225.53\sqrt{mk_B T}/b_x^2$. The simulations are run for a total duration of approximately 113.64τ with a time step $\Delta t = 2.27 \times 10^{-5}\tau$.

In simulations, we set $K_{el}^3 = 10^4 k_B T$, which is large enough to prevent significant twisting of flagella during rotation. $K_{el}^1 = K_{el}^2$ are set in the range between $2 \times 10^3 k_B T$ and $5 \times 10^4 k_B T$, corresponding to bending stiffnesses $K_{flag} = K_{el}^1 b_x$ between 1.7×10^{-23} Nm^2 and 4.2×10^{-22} Nm^2 . These values are within the range of experimentally measured bending stiffnesses 10^{-24} – 10^{-21} Nm^2 [40]. Furthermore, $\Omega_e^1 = 0.122$, $\Omega_e^2 = -0.027$ and $\Omega_e^3 = -0.217$, defining a left-handed helix in equilibrium with a radius of $0.23 \mu\text{m}$ and a pitch length of $2.56 \mu\text{m}$ [11]. Each flagellum consists of $N_s = 76$ segments, resulting in three helical turns. A basic *E. coli* model has five flagella, with one attached at one body end and four attached symmetrically to the side closer to the end (figure 2a). All flagella are actuated by a constant torque T_m applied to the first segment of flagellum structure. Note that for real *E. coli*, the motor torque may depend on the hydrodynamic load [55,56] and is not a control parameter directly, but here, to keep numerical simulations simple, we chose to keep T_m constant.

The body of *E. coli* is discretized by $N_v = 1278$ particles. The corresponding surface has a shear modulus of $\mu_0 = 8.1 \times 10^4 k_B T/b_x^2$ and the bending modulus $\kappa = 100k_B T$. The area and volume constraints assume $k_d = 8.1 \times 10^4 k_B T/b_x^2$, $k_a = 4.05 \times 10^4 k_B T/b_x^2$ and $k_v = 3.65 \times 10^5 k_B T/b_x^3$, with the body area $A_0^{\text{tot}} = 4.21b_x^2$ and the body volume $V_0^{\text{tot}} = 0.62b_x^3$. Excluded-volume interactions between the body and flagella or between different flagella are implemented through the LJ potential with parameters $\epsilon_{\text{LJ}} = k_B T$ and $\sigma_{\text{LJ}} = 0.07b_x$. Coupling between the *E. coli* model and fluid flow is imposed through DPD interactions with the parameters $a = 0$, $\gamma = 360\sqrt{mk_B T}/b_x$, $s = 0.1$ and $r_c = 0.09b_x$. A characteristic Reynolds number $Re = b_x m n_d v / \eta \approx 0.01$ is small enough to neglect inertial effects. Here, $v \approx 5.22 \times 10^{-3} \sqrt{k_B T/m} = 0.077b_x \tau^{-1}$ is the swimming speed of *E. coli*.

Simulations are carried out in two steps. First, *E. coli* with initially unbundled flagella (all rotating anti-clockwise) is let to swim and form a tight bundle due to hydrodynamic attraction between them [13,14,17,18]. Subsequently, we alternate between the run phase with all flagella rotating anti-clockwise and the tumble phase when one or two pre-selected flagella switch to the clockwise rotation by altering the torque direction. The run phase takes about 18.9τ and the tumble phase approximately 12.6τ , so that the duration of each simulation corresponds to approximately three tumble events. Note that the time scale τ depends on the applied torque T_m to each flagellum. In most simulations, the pre-selected flagella are also subject to polymorphic transformation, where the flagellum helicity is changed from left-handed to right-handed. We employ a simplified version of polymorphic transformation

Table 1. *Escherichia coli* parameters used in simulations and measured experimentally with the corresponding references.

property	simulation	experiment	reference
body length (μm)	3.0	2.5 ± 0.6	[11]
body width (μm)	1.0	0.9 ± 0.6	[11]
flag. contour length (μm)	8.9	8.3 ± 2.0	[57]
flag. pitch length (μm)	2.6	2.2	[57]
flag. helix radius (μm)	0.2	0.2	[57]
flag. bending rigidity (Nm^2)	10^{-22}	$10^{-24} - 10^{-21}$	[40]
mean run time (s)	0.13	1.0	[6,11]
mean tumble time (s)	0.08	0.14 ± 0.08	[25]

with only two states, left-handed and right-handed helices with the same helix radius and pitch. The polymorphic transformation is implemented such that the parameters Ω_n^1 and Ω_n^2 are changed from their original values (representing a left-handed helix) to the same magnitudes with the opposite sign (representing a right-handed helix) in a linear fashion during time 0.76τ . When the tumble phase is completed, the pre-selected flagella are again subject to anti-clockwise rotation and the reverse polymorphic transformation (from a right-handed to a left-handed helix), leading to the formation of the flagellar bundle.

To compare simulation results with experimental observations, we assume the body length of $3 \mu\text{m}$ and the body diameter of $1 \mu\text{m}$ [11]. The period of bundle rotation during *E. coli* run is $\tau = 6.7 \times 10^{-3} \text{ s}$ with a rotation frequency of 150 Hz [11], which allows us to relate simulation and physical time scales. This means that each simulation corresponds to a duration of 0.76 s , with the run-and-tumble times of approximately 0.13 and 0.08 s , respectively. Note that the run time of 0.13 s is shorter than typical *E. coli* run times of about 1 s , which has been selected to reduce computational cost, since we primarily focus on *E. coli* tumbling. However, the time of 0.13 s is long enough to form a tight flagellar bundle after a tumbling event. Ambient conditions correspond to a temperature of $T = 20^\circ\text{C}$ with the fluid viscosity of $\eta = 10^{-3} \text{ Pa s}$. Table 1 compares the properties of simulated and real *E. coli*.

2.4. Experimental methods and protocols

Escherichia coli strains used in the experiments are mutant strains AD62 and AD63. Both were genetically modified to express green fluorescent protein (GFP) in their body, while the flagella are specifically labelled with a fluorescent protein Alexa 647. This two-colour technique prevents signal overlap and enables a distinct simultaneous observation of both the bacterial body (green) and flagella (red) via our original 3D Lagrangian tracking technique [43]. From the perspective of run-and-tumble motility, AD62 corresponds to a standard wild-type *E. coli*. It was used to visualize the tumbling dynamics. AD63 is a ΔCheY mutant of AD62 that does not tumble ('smooth-runner'). It was used to study the relation between swimming velocity and the number of flagella. For this last experiment, each bacterium was tracked individually at a surface using a single colour (GFP) for a time long enough (around 50 s) to obtain a precise measurement of the swimming velocity. After that, a UV light was shone directly on the bacterium to obtain enough photo damage (after about 100 s), so that it stops the motion and triggers a full debundling of the flagella. The second colour excitation is then triggered to visualize and count the flagella individually.

The Lagrangian tracking device comprises two superimposed stages mounted on an inverted epifluorescence microscope (Zeiss Observer Z1, equipped with a C-Apochromat $63 \times 1.2 \text{ W}$ objective). The horizontal (x, y) position is controlled mechanically, and the z position is adjusted using a piezo-electric mover. A targeted fluorescent bacterial body is visualized within a 'trapping area' using a CCD camera. To synchronize image acquisition with stage movements, the stages and camera are triggered by a National Instruments TTL trigger module. The acquired images are transferred to a LabVIEW program, which processes the data. The program records the current x, y and z positions and directs the mechanical and piezoelectric stages to adjust accordingly, ensuring that the particle remains within the 'trapping area' and in focus [58].

Furthermore, to simultaneously image both the fluorescent body and the flagella, a two-colour LED light source (Zeiss Colibri 7) and a dichroic image splitter (Hamamatsu) are utilized to project two monochrome images onto separate regions of the camera chip. The microscope stage movement is computer-controlled to maintain the selected bacterium in focus, with images (1024×1024 pixels) captured at 80 frames per second using a Hamamatsu ORCA-Flash 4.0C11440 camera. The green and red images are subsequently superimposed to generate a movie depicting the tracked bacterium and its flagellar bundle (see electronic supplementary material, video S1). Due to photobleaching, flagella imaging is limited to approximately 1 min , but the timing of the second colour channel's application can be controlled to visualize flagella dynamics as needed [43].

The bacterial suspension must be dilute enough to avoid frequent bacterial collisions and is prepared according to the following protocol. Bacteria are inoculated in 10 ml of Luria Broth containing ampicillin at a concentration of $100 \mu\text{g ml}^{-1}$ and incubated overnight at 30°C . Subsequently, $100 \mu\text{l}$ of this culture is transferred into 10 ml of Tryptone Broth and incubated for several hours until the bacteria reach the early stationary phase. The bacteria are then harvested by centrifugation, and the supernatant is discarded. The pellet is resuspended in 1 ml of Berg Motility Buffer (BMB: $6.2 \text{ mM K}_2\text{HPO}_4$, $3.8 \text{ mM M}_2\text{PO}_4$, 67 mM NaCl and 0.1 mM EDTA) containing $10 \mu\text{l}$ of Alexa Fluor 647 red dye (prepared as a 5 mg ml^{-1} stock solution in dimethyl sulfoxide). The suspension is gently shaken for 2 h . Following this 2 h dyeing process on the bacterial flagella, the cells are washed again by centrifugation. The

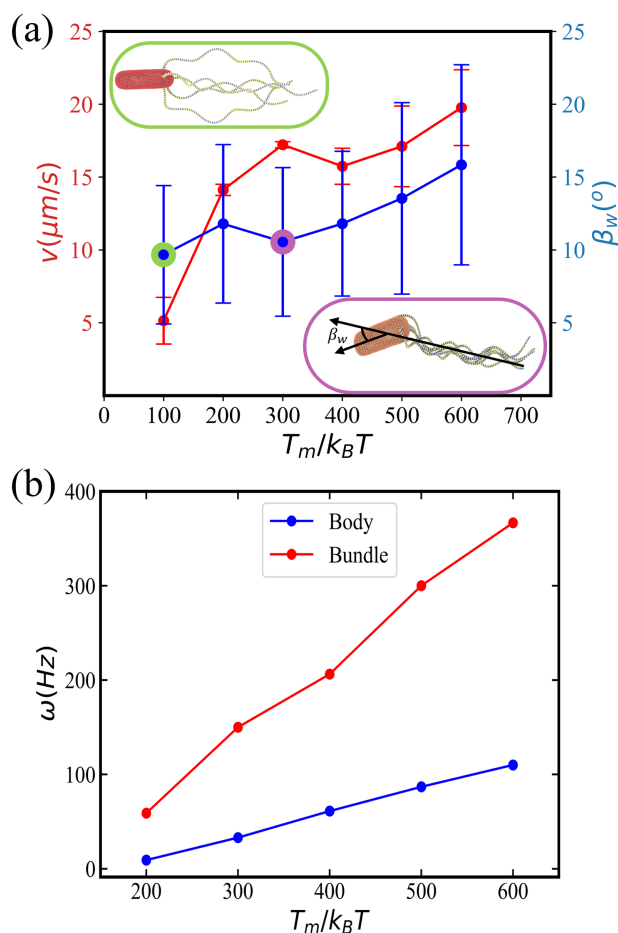


Figure 3. Five flagella *E. coli* model for different values of torque. (a) Average swimming speed v and wobbling angle β_w as a function of applied torque T_m . The swimming speed is computed from a fixed-time displacement and the wobbling angle is defined as the angle between the orientation vector of the body and the axis of flagellar bundle (see the inset at the bottom) during forward swimming (i.e. run phase). The error bars represent s.d. of a number of measurements performed during a run phase of about 1 s. Insets show snapshots of *E. coli* for the applied torques $T_m = 100 k_B T$ (top) and $T_m = 300 k_B T$ (bottom) with a poorly formed and tight flagellar bundle, respectively (see also electronic supplementary material, videos S2 and S3). (b) Rotation frequencies of the body and the bundle as a function of torque. The rotational frequencies are computed over the whole simulation time, where the number of rotations of the body or flagella bundle is divided by the total simulation time.

supernatant is then removed, and the final pellet is resuspended in a specific volume of BMB solution (with 0.08 g ml^{-1} L-serine) to maintain the activity of bacteria and inhibit bacterial division. Polyvinyl pyrrolidone (PVP-40 kDa, 0.005%) is added to prevent bacteria from sticking to surfaces.

3. Results

3.1. Run phase

3.1.1. Flagellar bundle formation

During the run phase, when all flagella rotate anti-clockwise, they form a tight bundle due to the rotational flow field between them and body counter-rotation [13,14,16–18]. However, hydrodynamic interaction forces are relatively weak, and the formation of the bundle may not take place for small torques applied. Insets in figure 3a illustrate two snapshots of *E. coli* with $T_m = 300 k_B T$ and $T_m = 100 k_B T$, where a tight bundle is formed or does not form, respectively (see also electronic supplementary material, videos S2 and S3). Our simulations show that torques $T_m \gtrsim 200 k_B T$ lead to the successful formation of a tight bundle. Available experiments [11,37,59] report an estimation of T_m to be in the range between 300 and 1500 pN nm, which corresponds to the range between $75 k_B T$ and $375 k_B T$ for room temperature. Applied torques in simulations are somewhat larger than those measured experimentally due to model limitations. Note that the thickness of simulated flagella is about 90 nm, which is larger than that in experiments (20 nm). Hydrodynamic forces between thick flagella are expected to be weaker than those for thin flagella so that larger torques are required for bundle formation. Note that bundle formation requires flagella to have a finite bending rigidity, since rigid helical structures would not be able to form a bundle. Furthermore, hook rigidity plays an important role in bundle formation, such that stiff hooks may prevent the formation of a bundle due to a preferred perpendicular orientation of flagella with respect to the body surface. This is consistent with experimental measurements that the hook is significantly softer than the rest of flagella [12,33,34].

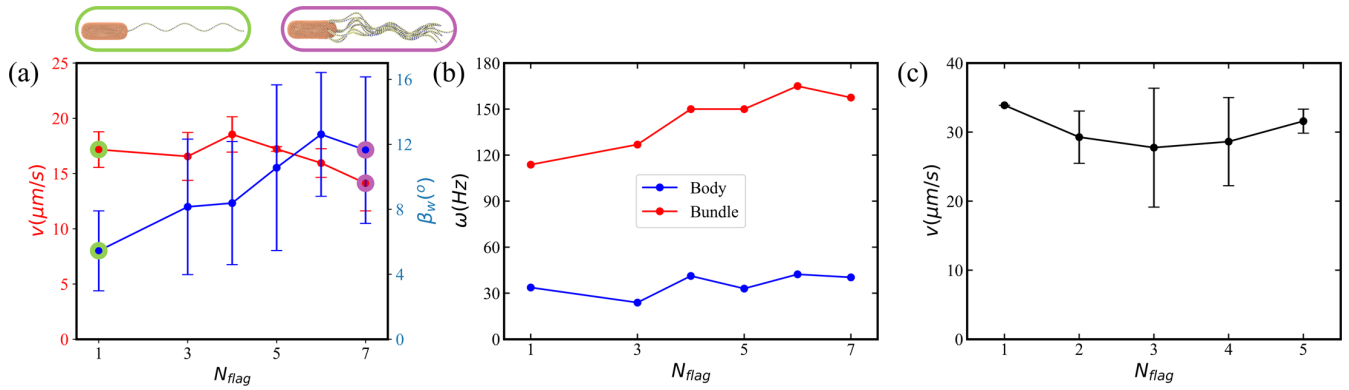


Figure 4. Dynamic properties of *E. coli* with different numbers of flagella ($N_{\text{flag}} = 1, 3-7$) during the run phase. $T_m = 300 k_B T$ in all cases. (a) Swimming speed v and wobbling angle β_w for a simulated *E. coli* as a function of the number of flagella (see electronic supplementary material, videos S4 and S5 for $N_{\text{flag}} = 1$ and $N_{\text{flag}} = 7$). (b) Simulated rotation frequencies ω of the body and the bundle for different N_{flag} . (c) Experimental measurements of *E. coli* swimming speed near a surface as a function of the flagella number (see §2.4 for practical details).

3.1.2. *Escherichia coli* propulsion as a function of applied torque

To quantify the run dynamics, we measure *E. coli* swimming speed v and wobbling angle β_w . The swimming speed is computed from a fixed-time displacement as $v = |\mathbf{r}(t_0 + \Delta t) - \mathbf{r}(t_0)| / \Delta t$, where $\mathbf{r}(t)$ is the centre of mass of *E. coli* at time t , and Δt is a fixed-time difference during which the bacterium does not change its swimming direction. We use $\Delta t = 22.8\tau$ (0.15 s) for simulations with the bacterium remaining in the run phase (i.e. no tumbling). The wobbling angle β_w corresponds to the angle between the body axis and a vector defined by the orientation of the bundle (see inset in figure 3a). β_w ranges from 0 to 90° and is sampled every 0.3τ (0.002 s) in time. Figure 3a shows the relationship between swimming speed and wobbling angle as a function of applied torque. The increase of speed with increasing torque is not linear. A large increase in v from $5 \mu\text{m s}^{-1}$ at $T_m = 100 k_B T$ to $15 \mu\text{m s}^{-1}$ at $T_m = 200 k_B T$ is due to the formation of a tight bundle at larger torques. For $T_m > 200 k_B T$, the increase in velocity is moderate and near linear as a function of torque. However, the wobbling angle also increases with increasing torque, which is expected to lead to increased fluid resistance [60]. Due to changes in β_w , an increase in the swimming speed may not necessarily be linear as a function of applied torque. The relatively large deviation in the wobbling angle in figure 3a is due to the fact that β_w regularly varies between zero and some maximum value. However, the averages of β_w should be reliable because they are based on a large number of samples (about 500).

Note that the swimming speed of $17.2 \mu\text{m s}^{-1}$ at $T_m = 300 k_B T$ is smaller than the average *E. coli* speed of $29 \pm 6 \mu\text{m s}^{-1}$ observed in experiments [11]. This difference might be due to several reasons. First, a finite size of the simulation domain results in a reduction of swimming speed, since the modelled bacterium interacts hydrodynamically with itself through periodic boundary conditions. However, much larger simulation domains quickly become very expensive computationally, which would significantly limit our study of *E. coli* tumbling. Second, the simulated flagella are thicker than real flagella, resulting in a slightly reduced propulsion strength. Such high resolution is difficult to achieve in our simulations due to a high computational cost.

Figure 3b presents rotation frequencies ω of the body and the bundle as a function of applied torque. As expected, both frequencies increase linearly with increasing T_m . A linear dependence of ω on T_m for both the body and the bundle suggests that body wobbling, which becomes larger with increasing torque (figure 3a), does not significantly affect the rotation frequencies. Experimentally measured values of ω are $23 \pm 8 \text{ Hz}$ for the body and $131 \pm 31 \text{ Hz}$ for the bundle [11], which agree well with ω values of 33 and 150 Hz in simulations for $T_m = 300 k_B T$. Therefore, the *E. coli* model with five flagella and $T_m = 300 k_B T$ is considered as a base model in further simulations.

3.1.3. *Escherichia coli* with different numbers of flagella

To test whether the number of flagella (typically between 2 and 7) affects dynamical characteristics of *E. coli*, we perform simulations for *E. coli* models with a different numbers of flagella. In all models, the arrangement of flagella is such that one flagellum is placed at the back along the long axis of the body, and the others are symmetrically placed at the selected circumference of the body surface. Figure 4a shows the swimming speed and the wobbling angle as a function of the number of flagella (see also electronic supplementary material, videos S4 and S5). The swimming speed remains nearly constant up to about five flagella and then slightly decreases for 6 and 7 flagella. A possible reason for the slight decrease in v is an increase in the wobbling angle with increasing number of flagella. Furthermore, our simulations indicate that the bundle becomes more spread with increasing number of flagella. Figure 4b presents rotational frequencies of the body and the bundle for different flagella numbers. The rotation of the body is nearly independent of the number of flagella, while the frequency of bundle rotation slightly increases. Despite the fact that the total applied torque is increased with increasing the number of flagella, rotational frequencies of the body and the bundle are primarily determined by how much torque is transferred to their rotation and how much is lost due to torques acting at different positions and in different directions (defined by the initial sections of flagella). Thus, rotational frequencies of the body and the bundle depend on T_m , the orientation and position of flagella motors, the number of flagella and the body geometry (see §3.2.1). In particular, the friction between flagella inside the bundle restricts higher rotation frequencies.

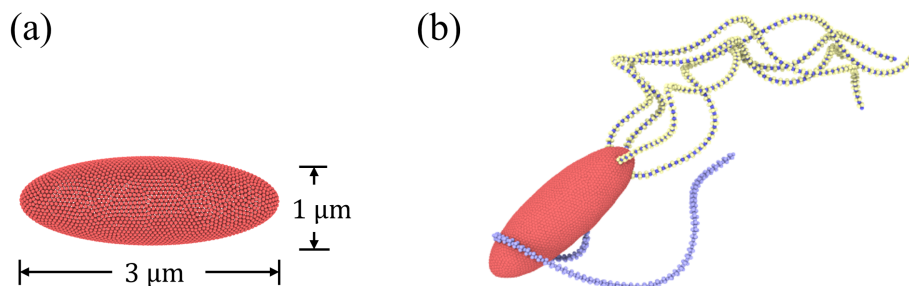


Figure 5. *Escherichia coli* model with a spheroidal body. (a) Dimensions of the body with a spheroidal shape. (b) Illustrative snapshot of a bacterium during tumbling (see also electronic supplementary material, video S6). Here, $N_{\text{flag}} = 5$, $K_{\text{flag}} = 2.7 \times 10^5 k_B T b_x$, $K_{\text{hook}} = 500 k_B T$ and $T_m = 300 k_B T$. The reverted flagellum does not undergo polymorphic transformation and hook stiffening.

For comparison, figure 4c shows the swimming speed of *E. coli* near a surface measured in experiments. The number of flagella was not changed directly, but counted *post-mortem* after the measurement of swimming velocity (see §2.4 for details). There is no obvious dependence of v on the number of flagella, which is consistent with our simulations and results in [61]. A simple theoretical argument to support this observation can be that the number of flagella primarily affects the thickness of the formed bundle (like a single thicker flagellum). Since the propulsion strength is expected to decrease weakly (i.e. logarithmic dependence) as a function of the bundle thickness, this effect might be very difficult to measure reliably. Furthermore, the slight increase in the bundle rotation frequency with increasing number of flagella in figure 4b may compensate for the expected decrease in the propulsion strength due to an increase in the bundle thickness. A recent study [61] also suggests a collective load sharing among multiple flagella, which results in a lower load on each flagellar motor and faster flagellar rotation. Note that it is not clear whether the overall output power of *E. coli* increases with the number of flagella. In our simulations, this is the case since each flagellum is driven by a constant torque of $T_m = 300 k_B T$. Despite the fact that the overall output power is increased in simulations with increasing the number of flagella, it has nearly negligible effect on the swimming speed.

3.2. Tumble phase

Next, we study systematically the tumble phase, focusing on the importance of various bacterium characteristics for a successful change in the swimming direction. Here, one of the flagella rotates clockwise, in contrast to the bundle formed by other flagella rotating anti-clockwise.

3.2.1. Effect of body shape

The shape of *E. coli* observed experimentally is generally spherocylinder-like (well described by equation (2.1) with $\nu = 8.5$) with some variation in the body length. This slender shape somewhat maximizes the body volume for a fixed length and aspect ratio. For comparison, we also consider a spheroidal body with the same dimensions defined by equation (2.1) with $\nu = 2$ (figure 5a). The *E. coli* model with the spheroidal body shape yields different rotation frequencies of the body and the bundle in the run phase (approx. 38 and 75 Hz, respectively), compared to the model with the spherocylinder-like body. This is primarily due to different angles of flagella attachment and different fluid frictions on the body during rotational motion. Note that for the spherocylinder-like body, the side flagella have a preferred orientation perpendicular to the body axis in equilibrium (figure 2a), while for the spheroidal body, the side flagella are partially aligned with the body axis. The ratio between bundle and body rotation frequencies significantly affects bacterium tumbling behaviour. For the spheroidal body, this ratio is close to two, so that the body rotation is relatively fast, often resulting in wrapping of the body by the clockwise-rotating flagella (figure 5b and electronic supplementary material, video S6). Occurrence of the wrapping leads to a very limited change in the swimming direction. For the spherocylinder-like body, this ratio is close to five [11], such that the clockwise-rotating flagella are able to leave the bundle without significant wrapping of the body, resulting in an efficient change of swimming direction. The wrapping of clockwise-rotating flagella around the body for the spheroidal case can be prevented by reducing the applied torque; however, much smaller torques significantly affect the bundle formation and the propulsion strength of *E. coli*.

3.2.2. Straight initial section of flagella

Flagellum geometry plays an important role in bundling and unbundling processes during the run-and-tumble phases [13,14,17,18]. We have tested the effect of a straight initial section of flagellum (i.e. no helicity) near the attachment point to the body (not a hook). Figure 6 compares the run-and-tumble phases of *E. coli* models with a varying length l_n (from 0 to about 26% of the contour length) of the linear flagellum section. In all cases, the formation of a tight bundle during the run phase is successful, though the initial section of the bundle is somewhat loose for the cases with a non-zero length of an initial straight section. However, the tumbling behaviour is significantly affected by the presence of a straight flagellum section, as can be seen from the snapshots in the bottom row in figure 6. Our simulations show that the clockwise-rotating flagellum has difficulties to leave the bundle for the initial straight sections of $l_n = 10$ –20 segments (13–26% of the contour length). This result suggests that the larger the differences between the clockwise-rotating flagellum and the bundle, the easier it is for it to leave the bundle. For the case of

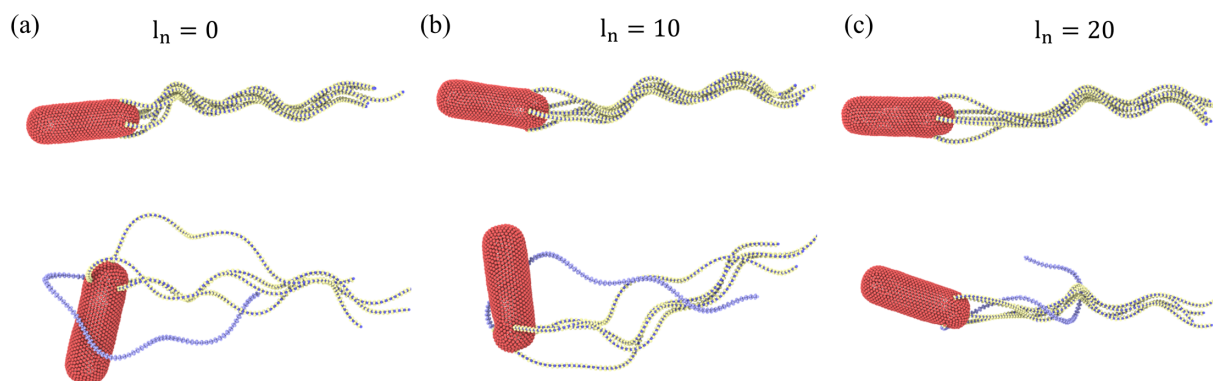


Figure 6. *Escherichia coli* models with a varying length of the linear flagellum section at the attachment to the body. (a) No initial linear section with full three turn left-handed helices. (b) An initial linear section of $l_n = 10$ segments (13% of the contour length). (c) An initial linear section of $l_n = 20$ segments (26% of the contour length). Snapshots in the top row show the run phase, while the bottom row illustrates the tumble phase. In all models, $N_{\text{flag}} = 5$, $K_{\text{flag}} = 2.7 \times 10^5 k_B T b_x$, $K_{\text{hook}} = 200 k_B T$ and $T_m = 300 k_B T$. In all three cases, no polymorphic transformation and hook stiffening are incorporated.

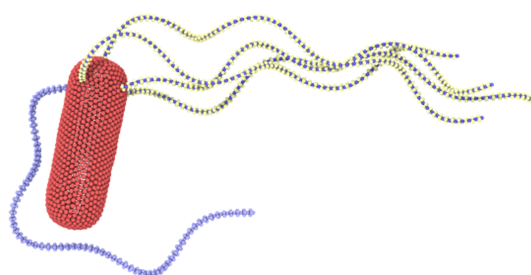


Figure 7. Tumble behaviour of *E. coli* with polymorphic transformation of the reverted flagellum (see also electronic supplementary material, video S7). Here, $N_{\text{flag}} = 5$, $K_{\text{flag}} = 2.7 \times 10^5 k_B T b_x$, $K_{\text{hook}} = 200 k_B T$ and $T_m = 300 k_B T$. Hook stiffening is not incorporated.

no initial straight section, the mismatch of rotation is present for the whole contour length, facilitating the easier escape of the clockwise-rotating flagellum from the bundle.

3.2.3. Polymorphic transformation

The snapshot of tumbling *E. coli* in figure 6a indicates that the bundle of anti-clockwise-rotating flagella becomes loose when the clockwise-rotating flagellum leaves the bundle. This means that the clockwise-rotating flagellum significantly disturbs the bundle. This appears to be different in experimental observations where the bundle generally remains tight during the tumble phase.

Several studies [11,25,26] report that the clockwise-rotating flagella of a wild-type *E. coli* are subject to the polymorphic transformation, during which the flagella change their helicity from left-handed to right-handed. We implement this transformation by gradually changing the sign of original values of Ω_n^1 and Ω_n^2 during a time of 0.76τ . An instant or very fast change of flagellar helicity is not stable in simulations. Figure 7 presents a snapshot of tumbling *E. coli* with polymorphic transformation, where the leaving flagellum has a smaller effect on the bundle, keeping its tight conformation (see also electronic supplementary material, video S7). At the end of the tumble phase, the reverted flagellum switches the rotation direction to anti-clockwise, performs the reverse polymorphic transformation (i.e. from the right-handed to left-handed helicity) and quickly joins the bundle.

The result that a polymorphic transformation of the clockwise-rotating flagella facilitates their efficient escape from the bundle without its significant disturbance can be understood as follows. A clockwise-rotating flagellum that leaves the bundle without polymorphic transformation exerts a propulsion force in the opposite-to-swimming direction, which competes with the propulsion force of the bundle. Since the propulsion forces from a single flagellum and a flagella bundle are comparable (supported by nearly independence of the swimming speed of *E. coli* on the number of flagella in figure 4), their counter-action in case of no polymorphic transformation of the clockwise-rotating flagellum leads to a significant slowdown of the bacterium and thus a partial disappearance of the bundle. However, in the case of polymorphic transformation, propulsion forces from this flagellum and the bundle act in a similar direction, so that the bacterium does not significantly lose its speed, maintaining a tight configuration of the bundle. Furthermore, we find that the clockwise-rotating flagellum with polymorphic transformation does not attract the counter-rotating bundle hydrodynamically, further facilitating its efficient escape from the bundle.

3.2.4. Stiffening of the hook during tumbling

Several recent studies [36,37] suggest that the hook of a reverted flagellum becomes dynamically stiffer when it starts rotating clockwise. Simulations with a fully flexible hook (i.e. $K_{\text{hook}} = 0$) lead to a poor tumbling of *E. coli* because the initial section of the reverted flagellum is nearly aligned with the body surface (figure 8a). Even though the reverted flagellum may separate from the bundle, it does not succeed in going sufficiently away from the bundle to significantly change the swimming direction. When the

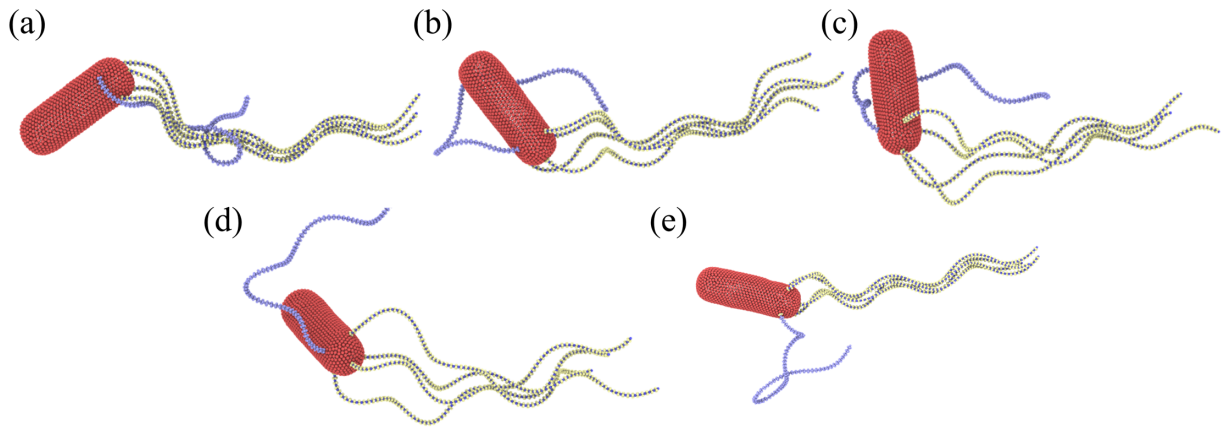


Figure 8. Tumble behaviour of *E. coli* models with different hook rigidities. (a) All flagella have a flexible hook with $K_{\text{hook}} = 0$. (b) All flagella with $K_{\text{hook}} = 100 k_B T$. (c) All flagella possess $K_{\text{hook}} = 200 k_B T$. (d) All flagella have a hook rigidity of $500 k_B T$. (e) A model where the reverted flagellum has $K_{\text{hook}} = 500 k_B T$, while the other flagella possess a hook rigidity of $100 k_B T$ (see also electronic supplementary material, video S8). In all cases, the polymorphic transformation of the clockwise-rotating flagellum is implemented. Here, $N_{\text{flag}} = 5$, $K_{\text{flag}} = 2.7 \times 10^5 k_B T b_x$ and $T_m = 300 k_B T$.

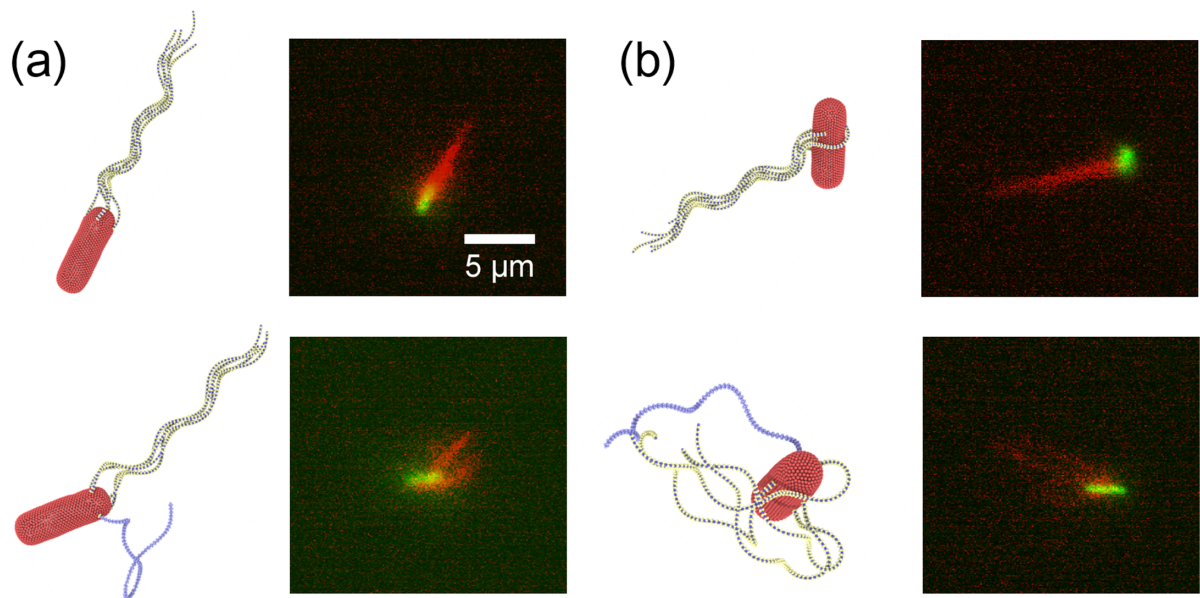


Figure 9. *Escherichia coli* models with different arrangements of flagella in comparison to experiments. (a) A symmetrical arrangement of flagella with one flagellum attached at the back along the body axis and the other four attached symmetrically at the body circumference with a 90° separation. In the experiment, the flagella are primarily located near one end of the body. See also electronic supplementary material, videos S8 and S10. (b) Random distribution of flagella attachment points on the whole body (see electronic supplementary material, videos S9 and S11). Snapshots in the top row show the run phase, while the bottom row illustrates the tumble phase. In simulations, $N_{\text{flag}} = 5$, $K_{\text{flag}} = 2.7 \times 10^5 k_B T b_x$, $T_m = 300 k_B T$ and the hook rigidity of the reverted flagellum is $500 k_B T$ with polymorphic transformation, while the other flagella have $K_{\text{hook}} = 100 k_B T$. The scale is the same in all experimental panels and is indicated by the scale bar of $5 \mu\text{m}$.

hook rigidity is increased, the situation drastically changes (figure 8b–e). Due to a preferred perpendicular orientation of the initial section of the reverted flagellum with respect to the body surface, its clockwise rotation pulls the flagellum out of the bundle. Furthermore, the hook rigidity drives the reverted flagellum towards a perpendicular-to-the-body orientation that is favourable for proper tumbling. However, hook stiffness can also be not too large, as it would then prevent the formation of a tight bundle.

Figure 8 shows tumbling *E. coli* models for several hook rigidities. As expected, the larger the hook rigidity is, the easier the reverted flagellum can leave the bundle. For $K_{\text{hook}} = 0$ in figure 8a, the reverted flagellum cannot efficiently leave the bundle. For $K_{\text{hook}} = 100 k_B T$ in figure 8b, orientation of the reverted flagellum is not well controlled, so that it partially wraps around the body. For $K_{\text{hook}} = 200 k_B T$ in figure 8c, orientation of the tumbling flagellum becomes better, but it still primarily remains near the bacterium body. Pronounced separation of the reverted flagellum is achieved for $K_{\text{hook}} = 500 k_B T$ in figure 8d; however, the bundle is relatively loose due to the large rigidity of flagella hooks. To incorporate hook stiffening due to different rotation directions into the model, we set $K_{\text{hook}} = 500 k_B T$ for the reverted flagellum and $K_{\text{hook}} = 100 k_B T$ for all other flagella. Figure 8e shows a tumbling event for this model, where a good separation of the reverted flagella with a minimum disturbance to the bundle is observed (see also electronic supplementary material, video S8). In conclusion, stiffening of the hook of the reverted flagella facilitates *E. coli* tumbling.

3.2.5. Different flagella arrangements

Escherichia coli bacteria in nature present a variety of flagella attachment locations ranging from their clustering near one end of the body to a random distribution over the whole body [37]. Figure 9 shows two *E. coli* models with different arrangements of flagella in comparison to experiments (see also electronic supplementary material, videos S8–S11). In all simulations, the total number of flagella is five. The symmetric placement of flagella we used so far (figure 9a) leads to persistent run dynamics of the bacterium with a moderate wobbling of the body, as shown in figure 3b. The symmetric model exhibits tumbling that compares well with experimental observations, if the flagella are primarily located near one end of the body (electronic supplementary material, videos S8 and S10). We have also tried a model with flagella randomly attached within the rear half of the body, which exhibits a comparable run phase but does not always reproduce successful tumbling, as the reverted flagellum does not always leave the bundle quickly enough. Finally, a random distribution of flagella attachment points on the whole body results in a strong wobbling of the body (figure 9b) with a reduction in the swimming speed. For this model, the tumble phase is also not well controlled, such that the change in the swimming direction ranges from small to large angles (electronic supplementary material, video S9). Similar run-and-tumble dynamics can also be found in experiments, as shown in figure 9b and electronic supplementary material, video S11. Available experimental observations indicate that all types of flagella arrangements are possible, though the majority of bacteria have them clustered near one end of the body. Note that the distribution of flagella attachment points can easily be adopted in simulations to reproduce the variety of *E. coli* tumbling dynamics in experiments.

3.2.6. Tumbling with several reverted flagella

Experimental observations suggest that more than one reverted flagella may be involved in the tumble phase. Figure 10 displays snapshots of tumbling *E. coli* models with one (figure 10a) and two (figure 10b) reverted flagella for different N_{flag} . Even though the tumbling behaviour is qualitatively similar in both cases, we can also observe some differences (electronic supplementary material, videos S8 and S12–S16). The major difference is that changes in the body and bundle orientations are more pronounced when two reverted flagella are activated, as shown in figure 11. This is not entirely surprising, since two reverted flagella exert larger torques on the body, enhancing dynamic changes in its orientation. Figure 10 also presents several experimental snapshots, which closely resemble simulation snapshots.

For a quantitative comparison, we employ the tumble angle β_{tumble} of *E. coli* shown in figure 11 for various N_{flag} . The tumble angle β_{tumble} is defined as the angle between the axis of the body before (i.e. in the run phase before tumbling) and after (i.e. when the bundle has formed again) a tumble event. For a single reverted flagellum, β_{tumble} decreases with increasing N_{flag} , as it becomes more difficult for the reverted flagellum to leave the bundle (figure 10a). Furthermore, a bundle with more flagella better controls the direction of the body, allowing smaller changes in its orientation. However, when two reverted flagella are involved in tumbling, β_{tumble} does not exhibit a monotonic dependence on N_{flag} , but it is larger than for a single reverted flagellum. Furthermore, tumbling angle is affected by the relative position of the reverted flagella on the body. Note that most of the tumble angles in simulations lie within the range of 30° – 90° experimentally observed values [6,11,25,38], which is indicated by the blue shaded area in figure 11.

3.2.7. Effect of flagella bending rigidity on tumbling

Since experimental measurements of flagella bending rigidity yield a rather wide range of 10^{-24} – 10^{-21} Nm² [40], we have also considered the possible effect of K_{flag} on the tumble angle β_{tumble} , shown in figure 12. Simulations indicate that *E. coli* with $K_{\text{flag}} = 1.8 \times 10^4 k_B T b_x$ does not exhibit a significant tumble behaviour with $\beta_{\text{tumble}} \approx 0$. For larger K_{flag} , β_{tumble} first decreases starting from relatively soft flagella with $K_{\text{flag}} = 4.5 \times 10^4 k_B T b_x$ to $K_{\text{flag}} = 2.7 \times 10^5 k_B T b_x$. For even larger K_{flag} , an increase in β_{tumble} is observed. Note that in the limit of rigid flagella, no bundle formation would be possible, even for a very flexible hook. As a result, *E. coli* flagella cannot be too soft or too stiff for a proper run-and-tumble behaviour.

4. Discussion and conclusions

Our main goals were to develop a realistic and flexible *E. coli* model and to address the question, of which physical properties of *E. coli* govern its run-and-tumble behaviour. We have identified a few parameters which strongly affect *E. coli* swimming behaviour, including the shape of the body and flagella, polymorphic transformation of flagella, dynamic hook stiffening and the arrangement of flagella on the body. It is a proper combination of these characteristics that makes *E. coli* an excellent swimmer, which can efficiently explore the surrounding environment.

An interesting result from both simulations and experiments is that the swimming speed is nearly independent of the number of flagella. Even though the total actuation power increases with increasing N_{flag} in simulations since each flagellum is driven by the same constant torque, the swimming velocity remains nearly unaffected. The rotation frequency of the bundle increases slightly with increasing N_{flag} ; however, the formed bundle appears to be less tight for a large number of flagella. Experimentally measured swimming velocities also appear to be independent of the number of flagella, though it is less clear whether the total actuation power increases with increasing N_{flag} or not. A possible explanation for this result can be that the number of flagella mainly affects the thickness of the formed bundle. Since the propulsion force depends logarithmically on the bundle thickness, it only weakly affects the swimming velocity. Furthermore, the existence of *E. coli* with implying that the ability different numbers of flagella suggests that there should not be significant evolutionary advantages of a specific number of flagella.

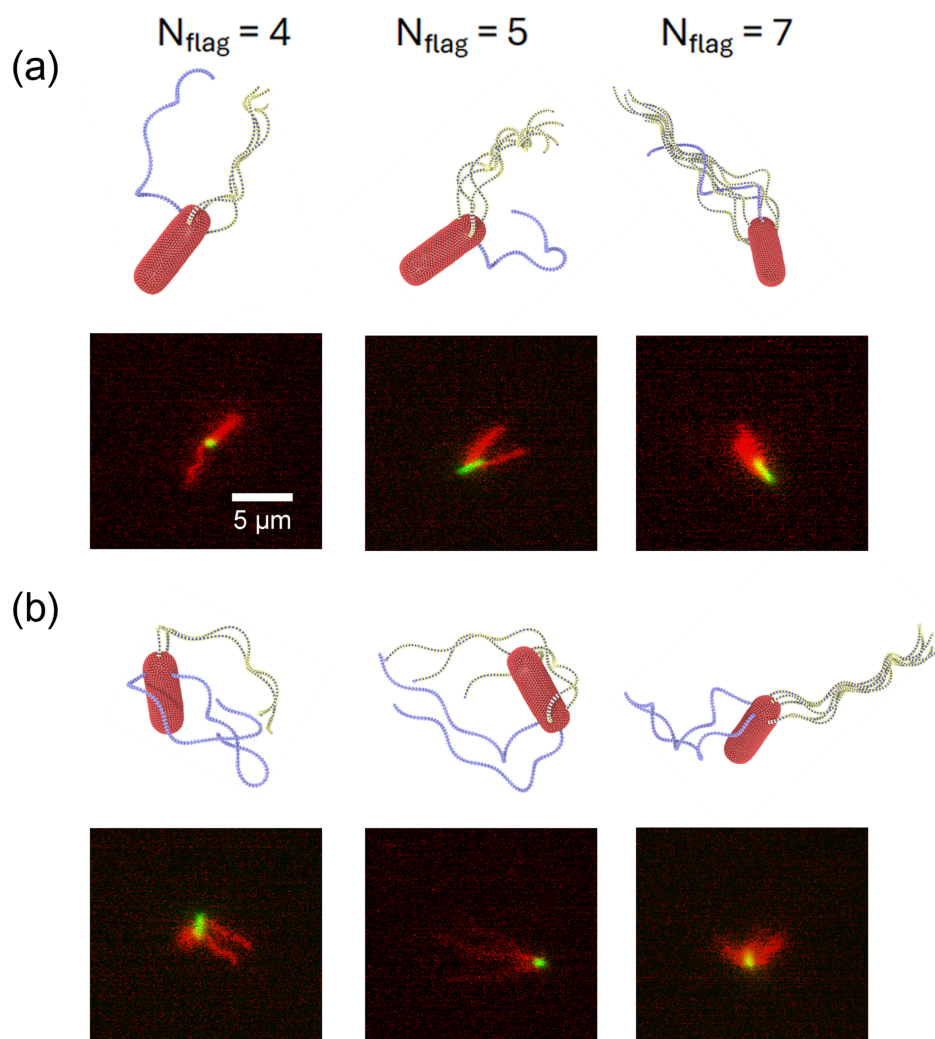


Figure 10. Tumble phase of *E. coli* models with different numbers of flagella. Snapshots of several cases with (a) one reverted flagellum and (b) two reverted flagella. For comparison, several experimental snapshots are also included next to the simulation snapshots. Note that N_{flag} values should be considered only for the simulation snapshots, as in the experimental observations, it is not possible to count the number of flagella. See also electronic supplementary material, videos S8 and S12–S16. In all simulations, $K_{\text{flag}} = 2.7 \times 10^5 k_B T b_x T_m = 300 k_B T$ and the hook rigidity of the reverted flagellum is $500 k_B T$ with polymorphic transformation, while the other flagella have $K_{\text{hook}} = 100 k_B T$. The scale is the same in all experimental panels and is indicated by the scale bar of $5 \mu\text{m}$.

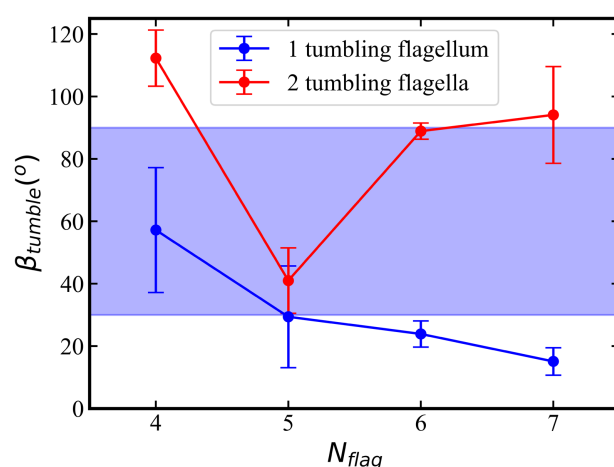


Figure 11. Tumble angles β_{tumble} of *E. coli* with different numbers of flagella (see snapshots in figure 10). The data are obtained from simulations with a symmetrical arrangement of flagella with one flagellum attached at the back along the body axis and the others attached symmetrically at the body circumference. The blue curve represents cases with one reverted flagellum, and the red curve corresponds to simulations with two reverted flagella. The blue shade indicates the range of tumble angles measured experimentally [11]. The tumble angle is defined as the angle between the orientation vector of the body before and after a tumble event. The error bars represent s.d.

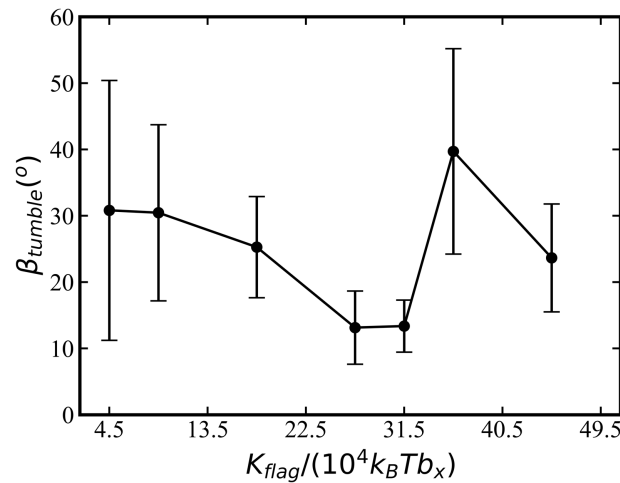


Figure 12. Tumble angle β_{tumble} of *E. coli* as a function of flagella bending stiffness. Here, only one reverted flagellum is employed with $N_{\text{flag}} = 5$. The tumble angle is defined as the angle between the orientation vector of the body before and after a tumble event. Each data point is averaged over three tumble events.

An important aspect is the ratio between rotational frequencies of the body and the flagellar bundle, which is close to 1/5 for a wild-type *E. coli*. During the run phase, the rotational frequency of flagellar bundle determines the swimming speed, while rotation of the body plays only a minor role. However, during the tumble phase, the rotational frequency of the body becomes important. When the body rotates fast, flagella that leave the bundle may quickly wrap around the body due to its rotation, limiting significantly the ability of a bacterium to change direction. Therefore, the ratio of 1/5 between the body and bundle rotation frequencies is small enough to facilitate the fast rotation of the bundle for a fast swimming speed and not to be detrimental for the tumble phase. For a spheroidal body in figure 5, this ratio is close to 1/2, implying that the ability for a bacterium to efficiently tumble with a not-very-fast rotation of the body imposes a much stronger constraint on the maximum rotation frequency of the bundle, and thus on the maximum swimming speed. Note that at low torques ($T_m \lesssim 200 k_B T$) of the actuating motors, the formation of a tight flagellar bundle is impeded due to weak hydrodynamic interactions, resulting in a reduced propulsion force of *E. coli*. Therefore, for efficient run-and-tumble behaviour, a proper balance between the body and bundle rotation is essential, which depends on geometric characteristics of the body and the bundle, the arrangement of the flagella and the value of the applied torque.

The other important physical property for an efficient *E. coli* tumbling is the polymorphic transformation of clockwise-rotating flagella that leave the bundle. Tumbling starts when one or several flagella switch the direction of rotation from anti-clockwise to clockwise. If the helicity of the clockwise-rotating flagella does not change, they start propelling against the swimming direction, leading to a substantial slowdown of *E. coli* and partial disruption of the tight bundle. As a result, the reverted flagella do not leave the bundle far enough to facilitate significant change in the swimming direction. However, when polymorphic transformation takes place and the reverted flagella change their helicity in addition to the change in the rotation direction, they exert propulsion forces in a direction close to the swimming direction, which does not significantly disturb the bundle. Furthermore, in this case, the reverted flagella and the bundle do not attract each other hydrodynamically, which facilitates the motion of the reverted flagella away from the bundle, resulting in an efficient change of the swimming direction.

A further important characteristic for *E. coli* tumbling is the bending rigidity of the hook, which controls the angle between the initial part of flagella and the body surface. For bundle formation during the run phase, flagella hooks have to be not too stiff, so that flagella can bend enough near their base and gather together into the bundle. However, the hook rigidity also plays a vital role in the tumble phase. Forces from a bent hook act to bring flagella to an orientation perpendicular to the body, aiding the reverted flagella to move away from the bundle. In fact, a recent experimental study [37] provides evidence that the bending rigidity of the hook is larger when flagella rotate clockwise in comparison to anti-clockwise rotation. This measurement suggests stiffening of the hook of reverted flagella, which has been considered in our simulations and has a positive effect on *E. coli* tumbling. Furthermore, the preference of a perpendicular orientation of flagella with respect to the body surface due to the hook bending rigidity affects its dynamics. Imagine a cable with torsional rigidity mounted perpendicular to a surface and bent along the surface. Rotation of this cable at the base would result first in pulling it along the surface due to torsional resistance until it bends enough near the base to allow the full rotation at the base. Note that if the mounting angle of the cable is not restricted (i.e. flexible attachment), the cable base would be aligned with the surface and its rotation at the base would simply lead to the rotation of the whole cable without any pulling effect. Similarly, reverted flagella attached to the cylindrical side of the body are first pulled out of the bundle, if the hook is not too soft, facilitating their escape from the bundle. Thus, these two effects (hook stiffening and initial pulling of reverted flagella) provided by the bending rigidity of the hook aid in the successful escape of the reverted flagella from the bundle.

Despite the fact that the developed *E. coli* model properly reproduces experimental observations and helps to explain the importance of different physical properties for bacterium dynamics, it should be best considered as a set of *E. coli* models. Large differences in *E. coli* behaviour have been found when different arrangements of flagella are considered. In fact, a substantial variety in run-and-tumble behaviour of *E. coli* is also observed in experiments, suggesting that structural properties of *E. coli* may have wide distributions. For our base model, we have selected $N_{\text{flag}} = 5$ symmetrically placed flagella at one of the body ends for simplicity. Random placement of flagella near one of the body ends yields a behaviour that is quite similar to that with the

symmetric placement of flagella. However, random distribution of flagella attachment points at the whole surface of the body results in a run-and-tumble behaviour, which strongly differs from that exhibited by the base model. Systematic characterization of *E. coli* behaviour for all combinations of parameters is currently not feasible due to high dimensionality of the parameter space. Furthermore, the behaviour of *E. coli* should be considered in a statistical fashion, since each tumbling event is different even for the base model with symmetrically placed flagella. For instance, a few tumbling attempts in simulations with the base model were not successful, as the reverted flagellum was not able to leave the bundle.

In the future, this model can be applied to address some questions related to the behaviour of *E. coli* and other peritrichous bacteria in complex environments, where experimental observations may not be detailed enough to propose corresponding physical mechanisms. For example, a recent experimental investigation [43] suggests that *E. coli* tumbling is necessary for a bacterium to escape from the wall, while the underlying physical mechanism is not clear. Another example, where our model can aid in the clarification of involved physical mechanisms, is *E. coli* swimming within soft confinements, such as lipid vesicles, leading to the formation of thin membrane tethers and overall vesicle transport by the encapsulated bacteria [62].

Ethics. This work did not require ethical approval from a human subject or animal welfare committee.

Data accessibility. All data, simulation code and analysing scripts are either within the article or available on Zenodo [63].

Electronic supplementary material is available online [64].

Declaration of AI use. We used AI-assisted technologies for editing the first draft of this article.

Authors' contributions. B.W.-Z.: data curation, formal analysis, investigation, methodology, visualization, writing—original draft; P.Z.: data curation, formal analysis, investigation, writing—original draft; R.B.: data curation, formal analysis; A.L.: funding acquisition, project administration, supervision, writing—review and editing; E.C.: funding acquisition, project administration, supervision, writing—review and editing; G.G.: conceptualization, funding acquisition, writing—review and editing; D.F.: conceptualization, methodology, project administration, software, supervision, writing—review and editing.

All authors gave final approval for publication and agreed to be held accountable for the work performed therein.

Conflict of interests. We declare we have no competing interests.

Funding. We acknowledge funding from the ETN 'Physics of microbial motility' (PHYMOT) within the European Union's Horizon 2020 research and innovation programme under Marie Skłodowska-Curie grant agreement no. 955910. R.B., A.L. and E.C. acknowledge the ANR-22-CE30 grant-Push-pull. A.L. and E.C. are supported by the Institut Universitaire de France.

Acknowledgements. B.W.-Z., G.G. and D.A.F. gratefully acknowledge computing time on the supercomputer JURECA [65] at Forschungszentrum Jülich under grant no. actsys.

References

- Elgeti J, Winkler RG, Gompper G. 2015 Physics of microswimmers—single particle motion and collective behavior: a review. *Rep. Prog. Phys.* **78**, 056601. (doi:10.1088/0034-4885/78/5/056601)
- Lauga E, Powers TR. 2009 The hydrodynamics of swimming microorganisms. *Rep. Prog. Phys.* **72**, 096601. (doi:10.1088/0034-4885/72/9/096601)
- Bechinger C, Di Leonardo R, Löwen H, Reichhardt C, Volpe G, Volpe G. 2016 Active particles in complex and crowded environments. *Rev. Mod. Phys.* **88**, 045006. (doi:10.1103/revmodphys.88.045006)
- Gompper G *et al.* 2025 The 2025 motile active matter roadmap. *J. Phys. Condens. Matter* **37**, 143501. (doi:10.1088/1361-648X/adac98)
- Gray J, Hancock GJ. 1955 The propulsion of sea-urchin spermatozoa. *J. Exp. Biol.* **32**, 802–814. (doi:10.1242/jeb.32.4.802)
- Berg HC, Brown DA. 1972 Chemotaxis in *Escherichia coli* analysed by three-dimensional tracking. *Nature* **239**, 500–504. (doi:10.1038/239500a0)
- Berg HC. 2003 The rotary motor of bacterial flagella. *Annu. Rev. Biochem.* **72**, 19–54. (doi:10.1146/annurev.biochem.72.121801.161737)
- Doughty M, Dryl S. 1981 Control of ciliary activity in *Paramecium*: an analysis of chemosensory transduction in a eukaryotic unicellular organism. *Prog. Neurobiol.* **16**, 1–115. (doi:10.1016/0301-0082(81)90008-3)
- Palagi S, Fischer P. 2018 Bioinspired microrobots. *Nat. Rev. Mater.* **3**, 113–124. (doi:10.1038/s41578-018-0016-9)
- Kaspar C, Ravoo BJ, van der Wiel WG, Wegner SV, Pernice WHP. 2021 The rise of intelligent matter. *Nature* **594**, 345–355. (doi:10.1038/s41586-021-03453-y)
- Darnton NC, Turner L, Rojevsky S, Berg HC. 2007 On torque and tumbling in swimming *Escherichia coli*. *J. Bacteriol.* **189**, 1756–1764. (doi:10.1128/jb.01501-06)
- Lee W, Kim Y, Griffith BE, Lim S. 2018 Bacterial flagellar bundling and unbundling via polymorphic transformations. *Phys. Rev. E* **98**, 052405. (doi:10.1103/physreve.98.052405)
- Kim M, Powers TR. 2004 Hydrodynamic interactions between rotating helices. *Phys. Rev. E* **69**, 061910. (doi:10.1103/physreve.69.061910)
- Reichert M, Stark H. 2005 Synchronization of rotating helices by hydrodynamic interactions. *Eur. Phys. J. E* **17**, 493–500. (doi:10.1140/epje/i2004-10152-7)
- Reigh SY, Winkler RG, Gompper G. 2013 Synchronization, slippage, and unbundling of driven helical flagella. *PLoS One* **8**, e70868. (doi:10.1371/journal.pone.0070868)
- Reigh SY, Winkler RG, Gompper G. 2012 Synchronization and bundling of anchored bacterial flagella. *Soft Matter* **8**, 4363. (doi:10.1039/c2sm07378a)
- Kim M, Bird JC, Van Parys AJ, Breuer KS, Powers TR. 2003 A macroscopic scale model of bacterial flagellar bundling. *Proc. Natl Acad. Sci. USA* **100**, 15481–15485. (doi:10.1073/pnas.2633596100)
- Kim MJ, Kim MJ, Bird JC, Park J, Powers TR, Breuer KS. 2004 Particle image velocimetry experiments on a macro-scale model for bacterial flagellar bundling. *Exp. Fluids* **37**, 782–788. (doi:10.1007/s00348-004-0848-5)
- Watarai N, Larson RG. 2010 The hydrodynamics of a run-and-tumble bacterium propelled by polymorphic helical flagella. *Biophys. J.* **98**, 12–17. (doi:10.1016/j.bpj.2009.09.044)
- Flores H, Lobaton E, Mendezdiez S, Tlupova S, Cortez R. 2005 A study of bacterial flagellar bundling. *Bull. Math. Biol.* **67**, 137–168. (doi:10.1016/j.bulm.2004.06.006)
- Janssen PJA, Graham MD. 2011 Coexistence of tight and loose bundled states in a model of bacterial flagellar dynamics. *Phys. Rev. E* **84**, 011910. (doi:10.1103/physreve.84.011910)
- Kanehl P, Ishikawa T. 2014 Fluid mechanics of swimming bacteria with multiple flagella. *Phys. Rev. E* **89**, 042704. (doi:10.1103/physreve.89.042704)
- Ishimoto K, Lauga E. 2019 The *N*-flagella problem: elastohydrodynamic motility transition of multi-flagellated bacteria. *Proc. R. Soc. A* **475**, 20180690. (doi:10.1098/rspa.2018.0690)
- Lauga E. 2016 Bacterial hydrodynamics. *Annu. Rev. Fluid Mech.* **48**, 105–130. (doi:10.1146/annurev-fluid-122414-034606)
- Turner L, Ryu WS, Berg HC. 2000 Real-time imaging of fluorescent flagellar filaments. *J. Bacteriol.* **182**, 2793–2801. (doi:10.1128/jb.182.10.2793-2801.2000)
- Berg HC. 2004 *E. coli in motion*. New York, NY: Springer.

27. Scharf B. 2002 Real-time imaging of fluorescent flagellar filaments of *Rhizobium lupini* H13-3: flagellar rotation and pH-induced polymorphic transitions. *J. Bacteriol.* **184**, 5979–5986. (doi:10.1128/jb.184.21.5979-5986.2002)
28. Berg HC, Purcell EM. 1977 Physics of chemoreception. *Biophys. J.* **20**, 193–219. (doi:10.1016/S0006-3495(77)85544-6)
29. Blair DF. 1995 How bacteria sense and swim. *Annu. Rev. Microbiol.* **49**, 489–522. (doi:10.1146/annurev.micro.49.1.489)
30. Vogel R, Stark H. 2012 Motor-driven bacterial flagella and buckling instabilities. *Eur. Phys. J. E* **35**, 15. (doi:10.1140/epje/i2012-12015-0)
31. Son K, Guasto JS, Stocker R. 2013 Bacteria can exploit a flagellar buckling instability to change direction. *Nat. Phys.* **9**, 494–498. (doi:10.1038/nphys2676)
32. Riley EE, Das D, Lauga E. 2018 Swimming of peritrichous bacteria is enabled by an elastohydrodynamic instability. *Sci. Rep.* **8**, 10728. (doi:10.1038/s41598-018-28319-8)
33. Brown MT, Steel BC, Silvestrin C, Wilkinson DA, Delalez NJ, Lumb CN, Obara B, Armitage JP, Berry RM. 2012 Flagellar hook flexibility is essential for bundle formation in swimming *Escherichia coli* cells. *J. Bacteriol.* **194**, 3495–3501. (doi:10.1128/jb.00209-12)
34. Nguyen FTM, Graham MD. 2018 Impacts of multiflagellarity on stability and speed of bacterial locomotion. *Phys. Rev. E* **98**, 042419. (doi:10.1103/physrev.98.042419)
35. Block SM, Blair DF, Berg HC. 1991 Compliance of bacterial polyhooks measured with optical tweezers. *Cytometry* **12**, 492–496. (doi:10.1002/cyto.990120605)
36. Nord AL, Biquet-Bisquert A, Abkarian M, Pigaglio T, Seduk F, Magalon A, Pedaci F. 2022 Dynamic stiffening of the flagellar hook. *Nat. Commun.* **13**, 2925. (doi:10.1038/s41467-022-30295-7)
37. Zhang X, Zhang C, Zhang R, Yuan J. 2023 Differential bending stiffness of the bacterial flagellar hook under counterclockwise and clockwise rotations. *Phys. Rev. Lett.* **130**, 138401. (doi:10.1103/physrevlett.130.138401)
38. Taute KM, Gude S, Tans SJ, Shimizu TS. 2015 High-throughput 3D tracking of bacteria on a standard phase contrast microscope. *Nat. Commun.* **6**, 8776. (doi:10.1038/ncomms9776)
39. Korobkova E, Emonet T, Vilar JMG, Shimizu TS, Cluzel P. 2004 From molecular noise to behavioural variability in a single bacterium. *Nature* **428**, 574–578. (doi:10.1038/nature02404)
40. Hu J, Yang M, Gompper G, Winkler RG. 2015 Modelling the mechanics and hydrodynamics of swimming *E. coli*. *Soft Matter* **11**, 7867–7876. (doi:10.1039/c5sm01678a)
41. Hu J, Wysocki A, Winkler RG, Gompper G. 2015 Physical sensing of surface properties by microswimmers—directing bacterial motion via wall slip. *Sci. Rep.* **5**, 9586. (doi:10.1038/srep09586)
42. Kong M, Wu Y, Li G, Larson RG. 2015 A bead-spring model for running and tumbling of flagellated swimmers: detailed predictions compared to experimental data for *E. coli*. *Soft Matter* **11**, 1572–1581. (doi:10.1039/c4sm02437k)
43. Junot G, Darnige T, Lindner A, Martinez VA, Arlt J, Dawson A, Poon WCK, Auradou H, Clément E. 2022 Run-to-tumble variability controls the surface residence times of *E. coli* bacteria. *Phys. Rev. Lett.* **128**, 248101. (doi:10.1103/physrevlett.128.248101)
44. Fedosov DA, Caswell B, Karniadakis GE. 2010 A multiscale red blood cell model with accurate mechanics, rheology, and dynamics. *Biophys. J.* **98**, 2215–2225. (doi:10.1016/j.bpj.2010.02.002)
45. Fedosov DA, Caswell B, Karniadakis GE. 2010 Systematic coarse-graining of spectrin-level red blood cell models. *Comput. Methods Appl. Mech. Eng.* **199**, 1937–1948. (doi:10.1016/j.cma.2010.02.001)
46. Helfrich W. 1973 Elastic properties of lipid bilayers: theory and possible experiments. *Z. Naturforsch.* **28**, 693–703.
47. Gompper G, Kroll DM. 1996 Random surface discretizations and the renormalization of the bending rigidity. *J. Phys. I Fr.* **6**, 1305–1320.
48. Gompper G, Kroll DM. 1997 Network models of fluid, hexatic and polymerized membranes. *J. Phys.* **9**, 8795–8834. (doi:10.1088/0953-8984/9/42/001)
49. Fedosov DA, Gompper G. 2014 White blood cell margination in microcirculation. *Soft Matter* **10**, 2961–2970. (doi:10.1039/c3sm52860j)
50. Wu-Zhang B, Fedosov DA, Gompper G. 2024 Collective behavior of squirmers in thin films. *Soft Matter* **20**, 5687–5702. (doi:10.1039/d4sm00075g)
51. Spöring I *et al.* 2018 Hook length of the bacterial flagellum is optimized for maximal stability of the flagellar bundle. *PLoS Biol.* **16**, e2006989. (doi:10.1371/journal.pbio.2006989)
52. Hoogerbrugge PJ, Koelman JMVA. 1992 Simulating microscopic hydrodynamic phenomena with dissipative particle dynamics. *Europhys. Lett.* **19**, 155–160. (doi:10.1209/0295-5075/19/3/001)
53. Español P, Warren P. 1995 Statistical mechanics of dissipative particle dynamics. *Europhys. Lett.* **30**, 191–196. (doi:10.1209/0295-5075/30/4/001)
54. Allen MP, Tildesley DJ. 1991 *Computer simulation of liquids*. New York, NY: Clarendon Press.
55. Berg HC, Turner L. 1993 Torque generated by the flagellar motor of *Escherichia coli*. *Biophys. J.* **65**, 2201–2216. (doi:10.1016/s0006-3495(93)81278-5)
56. Chen X, Berg HC. 2000 Torque-speed relationship of the flagellar rotary motor of *Escherichia coli*. *Biophys. J.* **78**, 1036–1041. (doi:10.1016/s0006-3495(00)76662-8)
57. Lee KY *et al.* 2018 Photosynthetic artificial organelles sustain and control ATP-dependent reactions in a protocellular system. *Nat. Biotechnol.* **36**, 530–535. (doi:10.1038/nbt.4140)
58. Darnige T, Figueroa-Morales N, Bohec P, Lindner A, Clément E. 2017 Lagrangian 3D tracking of fluorescent microscopic objects in motion. *Rev. Sci. Instrum.* **88**, 055106. (doi:10.1063/1.4982820)
59. Niu Y, Zhang R, Yuan J. 2023 Flagellar motors of swimming bacteria contain an incomplete set of stator units to ensure robust motility. *Sci. Adv.* **9**, eadi6724. (doi:10.1126/sciadv.adi6724)
60. Kamdar S, Shin S, Leishangthem P, Francis LF, Xu X, Cheng X. 2022 The colloidal nature of complex fluids enhances bacterial motility. *Nature* **603**, 819–823. (doi:10.1038/s41586-022-04509-3)
61. Kamdar S *et al.* 2023 Multiflagellarity leads to the size-independent swimming speed of peritrichous bacteria. *Proc. Natl Acad. Sci. USA* **120**, e2310952120. (doi:10.1073/pnas.2310952120)
62. Le Nagard L, Brown AT, Dawson A, Martinez VA, Poon WCK, Staykova M. 2022 Encapsulated bacteria deform lipid vesicles into flagellated swimmers. *Proc. Natl Acad. Sci. USA* **119**, e2206096119. (doi:10.1073/pnas.2206096119)
63. Fedosov D, Wu-Zhang B. 2025 Run-and-tumble dynamics of *E. coli* is governed by its mechanical properties—Data Availability. Zenodo. (doi:10.5281/zenodo.14618564)
64. Wu-Zhang B, Zhang P, Baillou R, Lindner A, Clement E, Gompper G *et al.* 2025 Supplementary material from: Run-and-tumble dynamics of *E. coli* is governed by its mechanical properties. Figshare. (doi:10.6084/m9.figshare.c.7742054)
65. Jülich Supercomputing Centre. 2021 JURECA: data centric and booster modules implementing the modular supercomputing architecture at Jülich supercomputing centre. *J. Large-Scale Res. Facil.* **7**, A182. (doi:10.17815/jlsrf-7-182)